Chinese Journal of
POLYMER SCIENCE

RESEARCH ARTICLE

https://doi.org/10.1007/s10118-026-3582-0
Chinese J. Polym. Sci.

Direct Ink Writing of Biodegradable Elastic Scaffolds *via* Rapid Thiol-Acrylate Photocrosslinking

Xiao-Yu Li[a], Chong-Guang Li[a], Kai Chen[a], Yan Xiao[a*], Xin-Xin Li[b*], and Mei-Dong Lang[a*]

[a] *Shanghai Key Laboratory of Advanced Polymeric Materials, Key Laboratory for Ultrafine Materials of Ministry of Education, School of Materials Science and Engineering, East China University of Science and Technology, Shanghai 200237, China*
[b] *Key Laboratory of Specially Functional Polymeric and Related Technology (Ministry of Education), School of Materials Science and Engineering, East China University of Science and Technology, Shanghai 200237, China*

Electronic Supplementary Information

Abstract Direct ink writing (DIW) has emerged as one of the most promising approaches for biomedical application, owing to its broad material compatibility, ease of operation, and high-resolution. However, the development of DIW inks with suitable rheological properties and excellent biocompatibility remains a significant challenge. Herein, an acrylate-functionalized liquid poly(4-methyl-ε-caprolactone) (PMCLDA) was synthesized as the precursor of 3D printing ink, accompanied with thiol-functionalized polyethylene glycol (PEGSH) as a rheological modifier. It was indicated from rheology study that the incorporation of PEGSH with PMCLDA precursor afforded the mixt inks shear thinning behavior. Moreover, it was verified by *in situ* Fourier transform infrared spectroscopy and photo-rheology that the mixed ink could rapidly cure through thiol-acrylate crosslinking under UV light. Various inks formulations were successfully utilized for printing 3D scaffolds *via* UV-assisted DIW, with the optimized printability for SH75 ink. Moreover, the 3D-printed scaffolds exhibited excellent elasticity and degradability. *In vitro* cytocompatibility assessments showed that the scaffolds exhibited good cytocompatibility and supported the proliferation of L929 mouse fibroblasts for a duration of 7 days. Therefore, it is demonstrated that the 3D-printed scaffolds crosslinked *via* thiol-acrylate crosslinking have great potential for applications in tissue engineering.

Keywords Thiol-acrylate crosslinking; Direct ink writing (DIW) printing; Elastic scaffold; Biodegradable material

Citation: Li, X. Y.; Li, C. G.; Chen, K.; Xiao, Y.; Li, X. X.; Lang, M. D. Direct ink writing of biodegradable elastic scaffolds *via* rapid thiol-acrylate photocrosslinking. *Chinese J. Polym. Sci.* https://doi.org/10.1007/s10118-026-3582-0

INTRODUCTION

Additive manufacturing (AM), an emerging fabrication technology based on layer-by-layer deposition of materials to construct three-dimensional structures, has been widely applied in tissue engineering and biomedical fields in recent years.[1–3] With the assistance of computer-aided design, AM enables precise control over material deposition, allowing for personalized customization and functional design of complex structures.[4,5] Various 3D printing techniques have been developed, including stereolithography (SLA),[6] digital light processing (DLP),[7,8] fused deposition modeling (FDM),[9,10] and direct ink writing (DIW).[11,12] Among these, DIW has emerged as one of the most promising techniques for fabricating tissue scaffolds owing to its broad material compatibility, ease of operation, multi-material printing capability, and high-resolution fabrication.[11] In DIW printing, inks are typically required to exhibit shear-thinning behavior to facilitate smooth extrusion through the nozzle, while curing rapidly after deposition, maintaining the printed shape, and supporting subsequent layers.[13,14] This places stringent requirements on both the rheological properties and curing performance of printing inks, particularly those based on synthetic polymers.[15] Therefore, achieving both printability and rapid solidification has become a critical challenge in the development of DIW inks.

Various strategies have been developed for improving the rheological properties of polymer-based DIW inks. You *et al*. reported a thickening method for thermosetting plastic polymers, in which sodium chloride particles were added to the precursor to increase ink viscosity. This approach provides sufficient mechanical support for the subsequent layers during the curing process and ensures the stability of the printed structure.[16] However, the printed scaffolds subsequently required additional thermal curing and prolonged immersion to remove sodium chloride particles, significantly extending the overall fabrication time. By contrast, photocurable systems enable rapid curing and shaping at room temperature.[17] For highly photoactive materials, ink can be

* Corresponding authors, E-mail: yxiao@ecust.edu.cn (Y.X.)
E-mail: xinxinli@ecust.edu.cn (X.X.L.)
E-mail: mdlang@ecust.edu.cn (M.D.L.)

Received December 21, 2025; Accepted January 20, 2026; Published online April 7, 2026

extruded from the nozzle and immediately cured *in situ* under UV light to form stable structures.[13,17] Gao *et al*. developed a methacrylate-functionalized polyurethane precursor for UV-assisted DIW of photocurable elastomers. In addition, SiO_2 nanoparticles were added to improve the rheological properties of the ink.[18] During printing, the ink was rapidly cured *via* acrylate homopolymerization to maintain its shape. However, the radical polymerization mechanism leads to stress concentration and volume shrinkage, which negatively affect the structural uniformity and mechanical properties of the resulting elastomer. In contrast, compared to acrylate homopolymerization, the introduction of thiols can effectively reduce the oxygen inhibition effect and improve network uniformity, offering a promising alternative for constructing crosslinked networks.[19–21]

In this study, an *in situ* thiol-acrylate photocrosslinking bioink was developed to optimize the rheological properties of UV-assisted DIW printing (Scheme 1). The precursor acrylate-functionalized liquid poly(4-methyl-ε-caprolactone) (PMCLDA) was used as the primary component of the printing ink. Its amorphous, liquid nature ensures stable extrudability during DIW printing while also exhibiting excellent cytocompatibility and biodegradability.[22–24] Thiol-functionalized PEGSH was simultaneously introduced as a rheological modifier at the same time. Rheological measurements were conducted to characterize the viscosity of mixed inks with varying formulations, while curing kinetics and reaction kinetics under UV irradiation were monitored *via in situ* photorheology and *in situ* FTIR, respectively. The effects of different PEGSH ratios on the properties of the crosslinked material were clarified by analyzing the network structure of the cured inks. Additionally, the printability of the ink was systematically evaluated to determine its suitability for precise 3D printing. Furthermore, the elasticity, degradability, and cytocompatibility of the printed scaffolds were comprehensively evaluated to verify their potential for application in tissue engineering and bioprinting.

EXPERIMENTAL

Materials

4-Methylcyclohexanone, *m*-chloroperoxybenzoic acid (*m*-CPBA) and 1,4-benzenedimethanol (BDM) were purchased from Merck. Polyethylene glycol PEG (average M_n=1000), Tin(II) 2-ethylhexanoate ($Sn(Oct)_2$), 3-mercaptopropionic acid, triethylamine, and acryloyl chloride were purchased from Adamas-beta. The photoinitiators ethyl (2,4,6-trimethylbenzoyl) phenylphosphinate (TPO-L) and poly(ε-caprolactone) (PCL, average M_n=8×10^4) were purchased from Aladdin. 4-Methylcyclohexanone was purified by vacuum distillation at 40 °C before use, while the others were used as received. CCK-8 test kit and cell viability staining solution was purchased from Beyotime.

Synthesis of Poly(4-methyl-ε-caprolactone) (PMCLDA)

In our previous work, the monomer 4-methyl-ε-caprolactone (MeCL) was synthesized *via* the Baeyer-Villiger oxidation reaction.[22] *m*-CPBA (120.00 g, 0.59 mol) was added to a reaction flask, followed by the addition of 500 mL of dichloromethane (DCM), and the mixture was stirred. Separately, purified 4-methylcyclohexanone (60.00 g, 0.53 mol) was dissolved in 150 mL of DCM and transferred to a 200 mL a constant pressure burette. The ketone solution was added dropwise to the oxidant solution at a rate of 1–2 drops per second under cooling in an ice-water bath. After complete addition, the mixture was stirred in an ice bath for an additional hour, followed by continuous reaction at room temperature for 24 h. Stirring was then stopped, and the excess solids were removed by filtration. The filtrate was successively washed with a saturated sodium thiosulfate solution, saturated sodium bicarbonate solution, and brine. The organic phase was then dried overnight over anhydrous magnesium sulfate. The solution was filtered to remove the drying agent and excess DCM was evaporated under reduced pressure to obtain the crude product. To the crude product, 1 g of calcium hydride (CaH_2) was added, and the mixture was stirred for 3 h. The final product was obtained by vacuum distillation at 110 °C to yield transparent oil. The purified MeCL was stored in dry

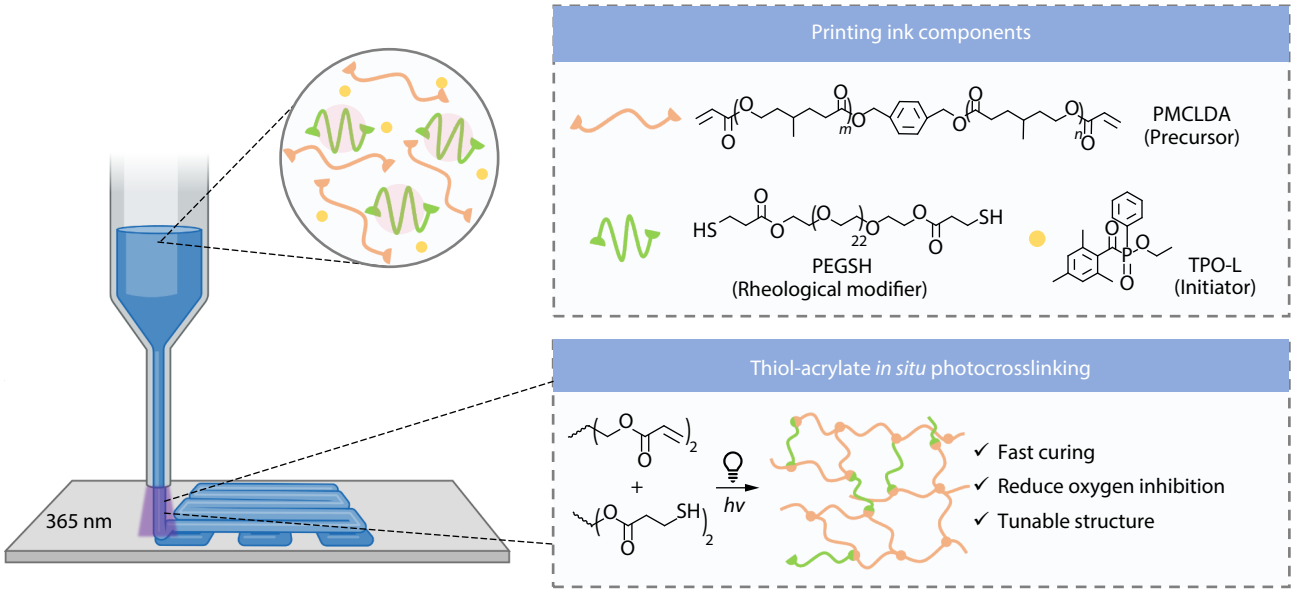

Scheme 1 Illustration of the DIW printing process, ink formulation and thiol-acrylate photocrosslinking mechanism.

https://doi.org/10.1007/s10118-026-3582-0

argon (yield: 90%). Poly(4-methyl-ε-caprolactone) (PMCL) was synthesized *via* ring-opening polymerization (ROP). Purified monomer MeCL (40.00 g, 0.31 mol) and initiator BDM (4.31 g, 0.031 mol) were added to a dry bottom flask and stirred. The mixture was heated to 60 °C under vacuum for 3 h to remove trace moisture. Then, $Sn(Oct)_2$ (40 mg, 0.1 wt% MeCL) was added to the flask under an argon atmosphere, and the reaction was carried out at 130 °C. After 24 h, the product was cooled to room temperature, diluted with DCM (5 mL), and precipitated into petroleum ether. The precipitated product was dried under vacuum to yield a light oil (yield: 90%).

Under an argon atmosphere, PMCL (13.00 g, 9.28 mmol) was added to a reaction flask under argon atmosphere. Subsequently, 80 mL of dry dichloromethane and triethylamine (TEA) (2.44 g, 24.14 mmol) were added and stirred. Acryloyl chloride (AC) (1.85 g, 20.43 mmol) and 50 mL dry dichloromethane were added to a constant pressure burette (molar ratio of PMCL:AC:TEA=1.0:1.1:1.3). The reaction was carried out in an ice-water bath, and acryloyl chloride solution was added dropwise at a rate of 1–2 drops per second. After the addition was complete, the reaction was continued for 1 h and then stirred at room temperature for 24 h. Upon completion of the reaction, anhydrous potassium carbonate was added and stirred for 3 h, after which the mixture was centrifuged to remove solids. Subsequently, 2 mL of hydrochloric acid (36%) was added and the mixture was stirred for 30 min, followed by dilution with dichloromethane to a total volume of 300 mL. The organic phase was washed successively with a saturated sodium bicarbonate solution and brine. The organic layer was collected, dried over anhydrous magnesium sulfate with stirring for 30 min, and allowed to stand. Solid magnesium sulfate was removed by filtration, and dichloromethane was removed under reduced pressure using rotary evaporation. The product was precipitated using petroleum ether and vacuum drying. Acrylate-functionalized PMCLDA was obtained and stored at –20 °C in the dark.

Synthesis of Viscosity Modifier Thiol Functionalized Poly(ethylene glycol) (PEGSH)

PEGSH was synthesized *via* a typical esterification reaction.[25] Poly(ethylene glycol) (PEGOH) (10.00 g, 10 mmol) and 3-mercaptopropionate (4.25 g, 40 mmol) were mixed in 100 mL of toluene. After complete dissolution, two drops of concentrated H_2SO_4 (98%) were added to the solution and stirring was continued. The solution was further heated to reflux, and the generated water was collected using a Dean-Stark trap. Heating was stopped when no more water was generated (approximately 20 h). The solution was cooled to room temperature, and excess toluene was removed by rotary evaporation. The resultant oil was dissolved in 200 mL of dichloromethane and washed with 50 mL of saturated $NaHCO_3$ solution and 50 mL of brine. The organic phase was dried over anhydrous $MgSO_4$ and concentrated to 20 mL by rotary evaporation. The solution was precipitated with cold diethyl ether and the resulting residue was dried under vacuum to yield a yellow oil. The dried product was purged with argon and stored at –20 °C (yield: 87%).

Preparation and Printing Process of 3D Printing Inks

Precursor PMCLDA and viscosity modifier PEGSH were added to a brown glass vial at five thiol-to-acrylate functional group molar ratios (0:1, 0.25:1, 0.5:1, 0.75:1 and 1:1). Subsequently, 1 wt% of the photoinitiator TPO-L was added, and the mixtures were stirred for 10 min, followed by sonication for 5 min, repeated three times to ensure homogeneous mixing. DIW printing was performed using a Biomaker 2i 3D printer with 3D models designed using the Biomaker software. An ultraviolet nozzle was selected, and a 25G nozzle (inner diameter of 0.25 mm) was used under 365 nm UV irradiation for printing. The irradiation intensity was 50 mW/cm^2. The nozzle and platform temperatures were set at 10 °C. Suitable printing parameters, including the nozzle temperature (T_{Nozzle}, °C), printing speed (mm/s), extrusion speed (mm^3/s), and layer height (mm), were optimized for each ink formulation. The mixed ink and corresponding scaffolds were labeled according to their thiol-to-acrylate ratios. For instance, mixed ink and the corresponding scaffolds with a thiol-to-acrylate ratio of 0.5:1 were denoted as the SH50 ink and SH50 scaffold, respectively. SH0 represented the ink without PEGSH and contained only PMCLDA and the photoinitiator.

In vitro Degradation of Scaffolds

For the *in vitro* degradation experiments, the scaffold samples were 3D printed grid scaffolds with dimensions of 10 mm × 10 mm × 2 mm. Each sample was immersed in PBS buffer (pH=7.4) containing 250 U/mL lipase and incubated in a shaking incubator at 37 °C with a shaking speed of 150 r/min.[26] PCL scaffold (M_n=8×10^4) (provided by our research group) was subjected to the same degradation conditions as the control.[27] The enzyme solution was replaced every two days. At predetermined time points, samples were collected, rinsed with deionized water, and freeze-dried to obtain degraded scaffolds (n=3). The change in dry mass was calculated using the following equation.

$$\text{Mass remains (\%)} = \frac{W_1}{W_0} \times 100\% \quad (1)$$

where W_1 represents the mass of the degraded sample, and W_0 represents the initial mass.

In vitro Cytocompatibility Assay

The cytotoxicity of 3D-printed scaffold extracts was evaluated on days 1, 3, and 7 using a Cell Counting Kit (CCK-8) cell viability assay. All scaffolds (5 mm × 5 mm × 2 mm) were sterilized by immersion in 75% ethanol for 24 h, followed by 2 h of UV irradiation (n=3). The sterilized scaffolds were then placed in 24-well plates and immersed in α-MEM supplemented with 10% FBS. A day before the experiment, 100 μL of freshly prepared L929 cell suspension (1.5×10^4 cells/well) was seeded in new 24-well plates. After culturing at 37 °C for 24 h, the medium was replaced with scaffold extracts, whereas the control group received α-MEM (10% FBS) without scaffolds. After an additional 24 h of incubation at 37 °C, the medium was removed and the wells were washed three times with PBS. The CCK-8 reagent was added at a ratio of 1:9 (reagent:medium), with 200 μL per well for the experimental group, control group, and blank wells. The plates were incubated at 37 °C in the dark for 1 h. Finally, 100 μL from each well was transferred to a clean 24-well plate and the absorbance at 450 nm was measured using a microplate reader (Thermo Scientific Multiskan FC). Cell viability was quantified using the following equation:

$$\text{Cell viability (\%)} = \frac{(OD_{sample} - OD_{blank})}{(OD_{control} - OD_{blank})} \times 100\% \quad (2)$$

where OD_{sample} represents the absorbance of the scaffolds, $OD_{control}$ represents the absorbance of the solution without scaffold, and OD_{blank} represents the absorbance of the blank wells.

To evaluate the effect of the scaffolds on L929 cell proliferation, SH75, SH50, and PCL scaffolds (5 mm × 5 mm × 2 mm) were placed in 24-well plates, and 250 μL of L929 cell suspension (1.5×10^4 cells/well) was added. PCL scaffolds (M_n=8×10^4) were used as a control group under identical culture conditions. After 1, 3, and 7 days of co-culture, the culture medium was removed, and the samples were washed three times with PBS. Subsequently, 200 μL of reaction solution (CCK-8: medium=1:9) was added to each well and incubated at 37 °C for 1 h in the dark. After incubation, 100 μL from each well was transferred to a new 24-well plate, and the absorbance at 450 nm was measured using a microplate reader (n=3). Live/dead staining was performed to evaluate the viability of the L929 cells on the scaffolds. The porous scaffolds were placed in 24-well plates (n=3) and seeded with L929 cells (1.5×10^4 cells per scaffold). On days 1, 3, and 7, scaffolds were washed with PBS, incubated in 200 μL PBS containing calcein AM (2 μL/mL) and propidium iodide (1 μL/mL) at 37 °C for 30 min in the dark, and rinsed with PBS. Cell viability was observed using confocal laser scanning microscopy (CLSM, Leica TCS SP8), with live cells displaying green fluorescence and dead cells displaying red fluorescence.

Characterization of PMCLDA, PEGSH and Mixed Inks

^{1}H-NMR spectra were recorded on a Bruker Avance 400 MHz NMR spectrometer using deuterated chloroform ($CDCl_3$) containing 0.03% tetramethylsilane (TMS) as the internal reference. Fourier transform infrared (FTIR) spectra were recorded on a Nicolet iS50 FTIR spectrometer using the KBr pellet method, with a spectral range of 400–4000 cm^{-1}. The number-average molecular weight (M_n) and molecular weight dispersity ($Đ$) of the polymers were determined by gel permeation chromatography (GPC) using a Waters 1515 instrument equipped with Tosoh TSK gel Alpha-2500 and Alpha-3000 columns. The sample solutions were prepared at a concentration of 2 mg/mL. The viscosities of the mixed inks were measured using a rotational rheometer (Hakke RheoStress 600). In the oscillatory mode, viscosity variation was recorded, while in the rotational continuous scanning mode, the viscosity dependence on shear rate (0.1–100 s^{-1}) was assessed. The tests were conducted at a fixed frequency of 1 Hz and temperature of 10 °C. Each sample was tested in triplicates.

Characterization of Reaction Kinetics

Real-time *in situ* FTIR studies were performed on a Nicolet is50 FTIR spectrometer. The mixed inks were placed in two NaCl crystals and vertically placed into the sample chamber. Irradiation intensities were measured with a DTGS KBr detector, and series scans were recorded at a rate of 1 scan/s. Thiol functional group conversion was monitored using the S—H absorption band at 2570 cm^{-1}, and acrylate functional group conversion was monitored using the C=C absorption bands at 1619 and 1636 cm^{-1}. A C=O tensile vibration band was observed at 1750 cm^{-1} as the internal standard band.[28] Polymerization was initiated *via* a 365 nm light source with an irradiation light intensity of 50 mW/cm^2. The intensity of the light source was calibrated using a 340–420 nm UV led-X_0 optical power meter (Linshang Technology, China). Data were acquired using the OMNIC software, and each group of samples was tested in triplicate.

In situ photorheology was performed using a HAAKE MARS 60 equipped with a parallel plate with a geometry of 20 mm. Photorheological measurements were conducted using a rheometer equipped with a UV-visible accessory. The shear oscillation mode was set at strain of 1%, frequency of 1 Hz, UV irradiation intensity of 50 mW/cm^2 and temperature of 10 °C. The test time was 5 min and each sample was tested in triplicate.

Characterization of Crosslinked Networks and Scaffolds

The mixed inks were cured under UV irradiation in a custom dumbbell-shaped mold to obtain crosslinked materials. The swelling ratio and gel fraction of the crosslinked networks were determined by immersing each sample in toluene for 24 h followed by vacuum drying at 60 °C for 24 h (n=3). The degrees of swelling and gel fraction were calculated using the following equations[29]:

$$\text{Gel fraction (\%)} = \frac{m_d}{m_i} \times 100\% \tag{3}$$

$$\text{Swelling ratio (\%)} = \frac{m_s - m_d}{m_i} \times 100\% \tag{4}$$

where m_d is the dry mass, m_s is the swollen mass, and m_i is the initial mass prior to swelling. The thermomechanical properties of the crosslinked networks (30 mm × 5 mm × 0.5 mm) were measured using dynamic mechanical analysis (DMA Q800). The temperature range was −80 to 150 °C, with a ramping rate of 3 °C/min using the extension mode (sinusoidal stress of 1 Hz frequency) under a nitrogen atmosphere with an amplitude of 10 μm. The average molecular weight between crosslinks (M_c) and crosslink density (V_e) were calculated using the following equations[30,31]:

$$M_c = \frac{3\rho RT}{E'_{T_g+50K}} \tag{5}$$

$$V_e = \frac{\rho}{M_c} \tag{6}$$

where ρ is the density of the materials, R is the gas constant (8.314 J/(K·mol)), T is the temperature at T_g+50 K, and E'_{T_g+50K} refers to the storage modules at T_g+50 K. The density, ρ of the crosslinked materials is determined using the water displacement method. Tensile tests were performed on a universal testing machine (Shanghai Kaiyan KY-250N) in the tensile mode at a speed of 10 mm/min. The sample dimensions were 30 mm × 5 mm × 0.5 mm, and each set of samples was tested in triplicate (n=3). The pore structures of the scaffolds and their morphologies after degradation were examined using a scanning electron microscope (FE-SEM S-3400). The perimeter and area of the scaffold pores were calculated from micrographs using the Image Pro Plus software. The printability (P_r) of the inks was evaluated using the following equation[32] (n=3):

$$P_r = \frac{L^2}{16A} \tag{7}$$

where L and A represent the perimeter and area of the scaffold pores, respectively.

Cyclic compression tests of the printed scaffolds (10 mm × 10 mm × 4 mm) were performed for 10 compression cycles in compression mode with a strain of 50% at a compression rate

of 5 mm/min. The glass transition temperatures (T_g) of the scaffolds were determined by differential scanning calorimetry (DSC, PerkinElmer DSC 8500) from –70 °C to 80 °C at a rate of 10 °C/min under a nitrogen atmosphere. The crystallization of the scaffolds was tested using an X-ray diffractometer (Bruker D8A XRD ECO) at 40 kV and 25 mA, with a scan rate of 5 °/min and a scattering angle range of 5°–60°. The hydrophilicity of the scaffolds was evaluated using a contact angle goniometer (JC2000D2) (n=3).

RESULTS AND DISCUSSION

Synthesis of Precursor PMCLDA and Viscosity Modified PEGSH

To obtain the main components of the printing ink, PMCLDA and PEGSH were separately synthesized (Fig. 1). As shown in Fig. 1(a), PMCL was synthesized *via* ring-opening polymerization (ROP) using BDM diol as the initiator. The terminal hydroxyl groups of PMCL were subsequently modified *via* an amidation reaction to obtain PMCLDA. The ^{1}H-NMR spectra of PMCL and PMCLDA were shown in Fig. 1(c). The degree of polymerization of the polymer was determined by quantifying the area ratio of peak *b* from the initiator to peak *d* from the MeCL monomer, which was consistent with the theoretical value. In addition, the appearance of characteristic peak *g* (5.72 ppm, —COOCH=C$\underline{H}_2$), peak *f* (5.98 ppm, —COOC$\underline{H}$=CH$_2$), and peak *h* (6.28 ppm, —COOCH=C$\underline{H}_2$) in the PMCLDA spectrum, along with the complete disappearance of the methylene peak *e′* (3.69 ppm, —CH$_2$C$\underline{H}_2$O—), indicate that the terminal groups of PMCL were successfully and completely modified. The appearance of the C=C stretching vibration absorption band at 1636 cm^{-1} in the FTIR spectrum further confirmed the successful synthesis of PMCLDA (Fig. S1a in the electronic supplementary information, ESI). The GPC curves show that both PMCL and PMCLDA exhibited monomodal distributions, reflecting a narrow molecular weight distribution and well-controlled polymer structure. (Fig. S1b in ESI).

PEGSH, as a viscosity modifier, was synthesized by esterification of PEGOH (Fig. 1b). The ^{1}H-NMR spectra of PEGOH and PEGSH are shown in Fig. 1(d). The appearance of characteristic peak *e* (1.69 ppm, —CH$_2$S$\underline{H}$), peak *d* (2.69 ppm, —C$\underline{H}_2$CH$_2$SH), *c* (2.79 ppm, —CH$_2$C$\underline{H}_2$SH—), and methylene peak *b′* at 4.27 ppm (—C$\underline{H}_2$COO—) confirmed the successful thiol modification of PEGOH. The complete modification of the PEGOH terminal groups was further confirmed by the peak area ratio of peak *e* to peak *b′*. Additionally, the FTIR spectrum shows an S—H stretching vibration absorption band at 2570 cm^{-1}, indicating the successful synthesis of PEGSH.

Properties of the Mixed Inks and Crosslinked Network

To investigate the effect of PEGSH on the ink viscosity, the synthesized PMCLDA and PEGSH were mixed at five different thiol-

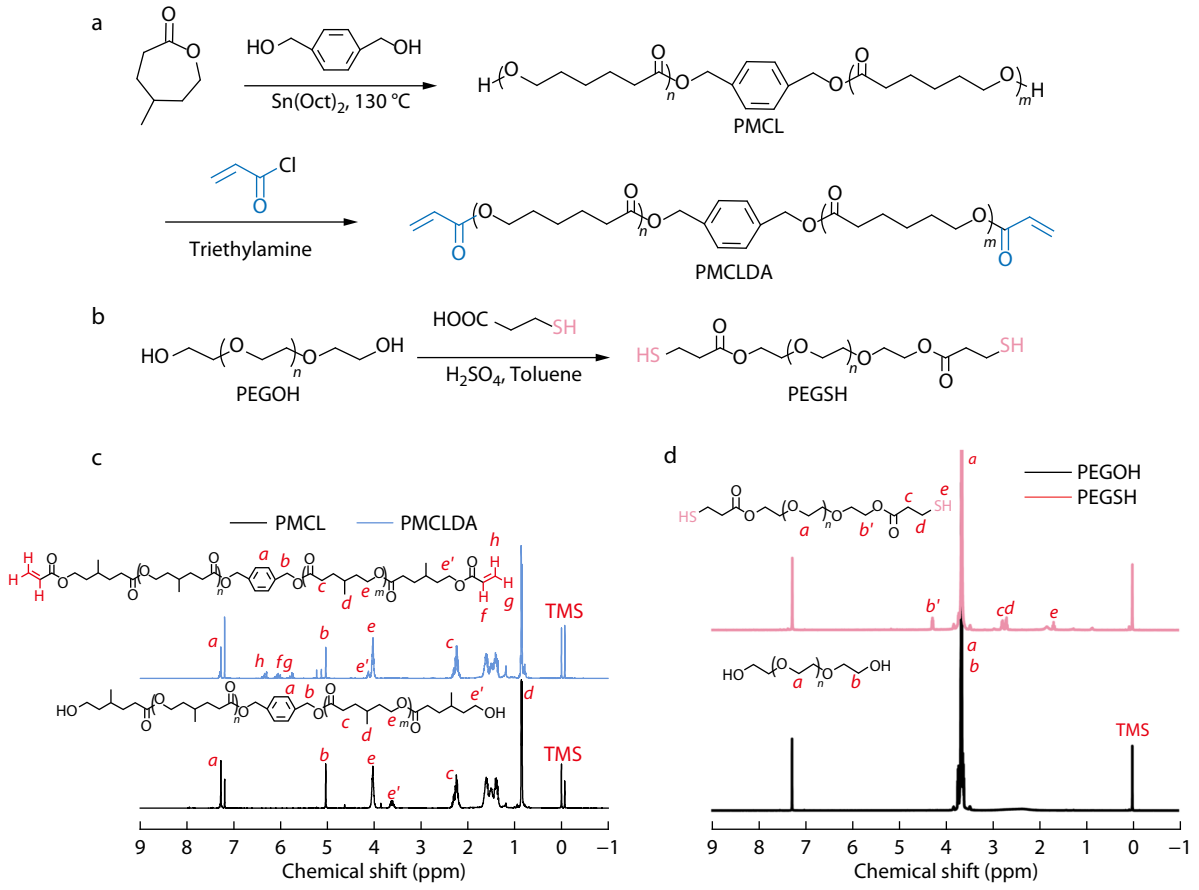

Fig. 1 Synthetic routes for (a) precursor PMCLDA and (b) rheology modifier PEGSH; (c) ^{1}H-NMR spectra of PMCL and PMCLDA; (d) ^{1}H-NMR spectra and PEGOH and PEGSH.

https://doi.org/10.1007/s10118-026-3582-0

to-acrylate ratios (0:1, 0.25:1, 0.5:1, 0.75:1, 1:1), respectively. The viscosities of the mixed inks SH0, SH25, SH50, SH75, and SH100 were characterized. Fig. 2(a) shows the viscosities of the different inks measured at 10 °C in oscillatory shear mode. The viscosity of the SH0 ink is only 2.1 Pa·s. As the PEGSH content in the mixture increased, the viscosity of the ink increased significantly, reaching a maximum of 889.4 Pa·s for SH100. The PEGSH is in a crystalline state at 10 °C with a crystallinity of 55% (Fig. S2 in ESI),[33] which explained the relatively low viscosity of the ink in the absence of PEGSH. When PEGSH was homogeneously mixed with amorphous PMCLDA, the crystalline structure of PEGSH restricted the molecular motion, thereby reducing the overall fluidity of the mixed ink. Furthermore, as the PEGSH content increased, the crystalline domains also increased, leading to higher ink viscosity.

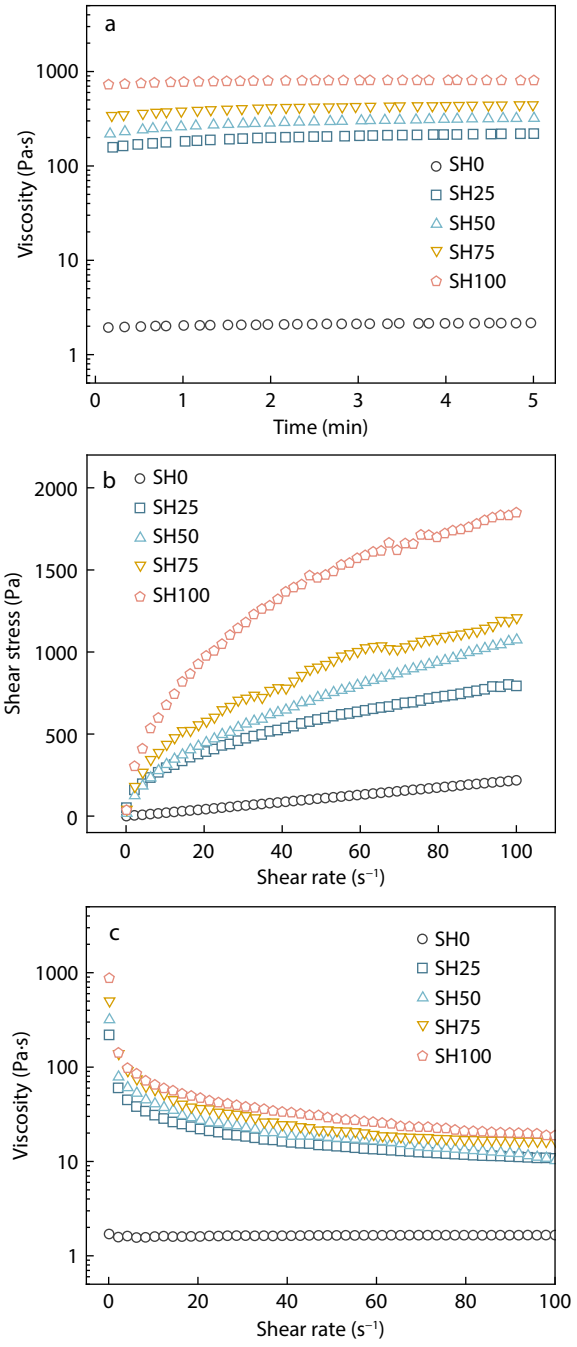

Fig. 2 Rheological studies of five different inks (SH0, SH25, SH50, SH75 and SH100). (a) The viscosity under oscillatory shear mode; (b) Shear stress varies with shear rate (0.01–100 s^{-1}) under continuous rotational scanning mode, and (c) viscosity varies with shear rate under continuous rotational scanning mode. The temperature was set at 10 °C.

To further investigate the rheological performance of inks with different ratios, the variation in ink viscosity with shear rate was measured in continuous rotational scanning mode. As shown in Figs. 2(b) and 2(c), as the shear rate increased from 0.01 s^{-1} to 100 s^{-1}, it could be observed that the shear stress exhibited a linear relationship with the shear rate for SH0, while the viscosity remained constant. This indicates that PMCLDA behaved as a Newtonian fluid. In contrast, for inks containing PEGSH, the shear stress increased linearly with the shear rate. The viscosity of the mixed inks decreased significantly under shear, exhibiting a pseudoplastic behavior. It was demonstrated that the addition of PEGSH effectively regulated the rheological performance of the PMCL, endowing the mixed inks with shear-thinning characteristics that facilitated smooth extrusion during printing.

Because the viscosity of ink decreases after extrusion, a slow curing rate may lead to material collapse or deformation during stacking, resulting in poor printing accuracy.[13] To investigate the curing process of different inks during printing, the photopolymerization and curing kinetics of the four mixed inks (SH25, SH50, SH75, and SH100) were monitored using *in situ* FTIR and *in situ* photorheology, respectively. By monitoring the changes in the band areas of S—H at 2570 cm^{-1} and the C=C peak at 1636 cm^{-1} in the FTIR spectra (Figs. S3 and S4 in ESI), the conversions of acrylate and thiol monomers were shown in Figs. 3(a) and 3(b). Upon UV irradiation, the acrylate and thiol groups converged immediately, showing no induction period during polymerization. The acrylate groups were fully converted for all four mixed inks. However, the thiol groups exhibited different behaviors depending on ink composition. In the case of SH25, the thiols were almost completely converted. In contrast, for SH50, SH75, and SH100, some thiols remained unreacted. Moreover, the final thiol conversion decreased as the PEGSH content of the inks increased. This was attributed to the occurrence of acrylate homopolymerization during thiol-acrylate photopolymerization, which led to an excess of thiols.[34] In addition, the acrylate functional groups were fully converted within 5 s in all four mixed inks. This rapid reaction facilitated rapid solidification during printing, ensuring the structural stability and printing precision of the scaffolds.

The curing kinetics of the mixed inks were further monitored using *in situ* rheology (Fig. S5 in ESI). As shown in Figs. 3(c) and 3(d), before UV irradiation, the loss modulus (G'') of the mixed ink was higher than its storage modulus (G'), exhibiting a characteristic viscous-dominated behavior. When the UV light was switched on, the storage modulus G' increases rapidly and was higher than the loss modulus G''. This indicated that thiol-acrylate polymerization occurred upon irradi-

https://doi.org/10.1007/s10118-026-3582-0

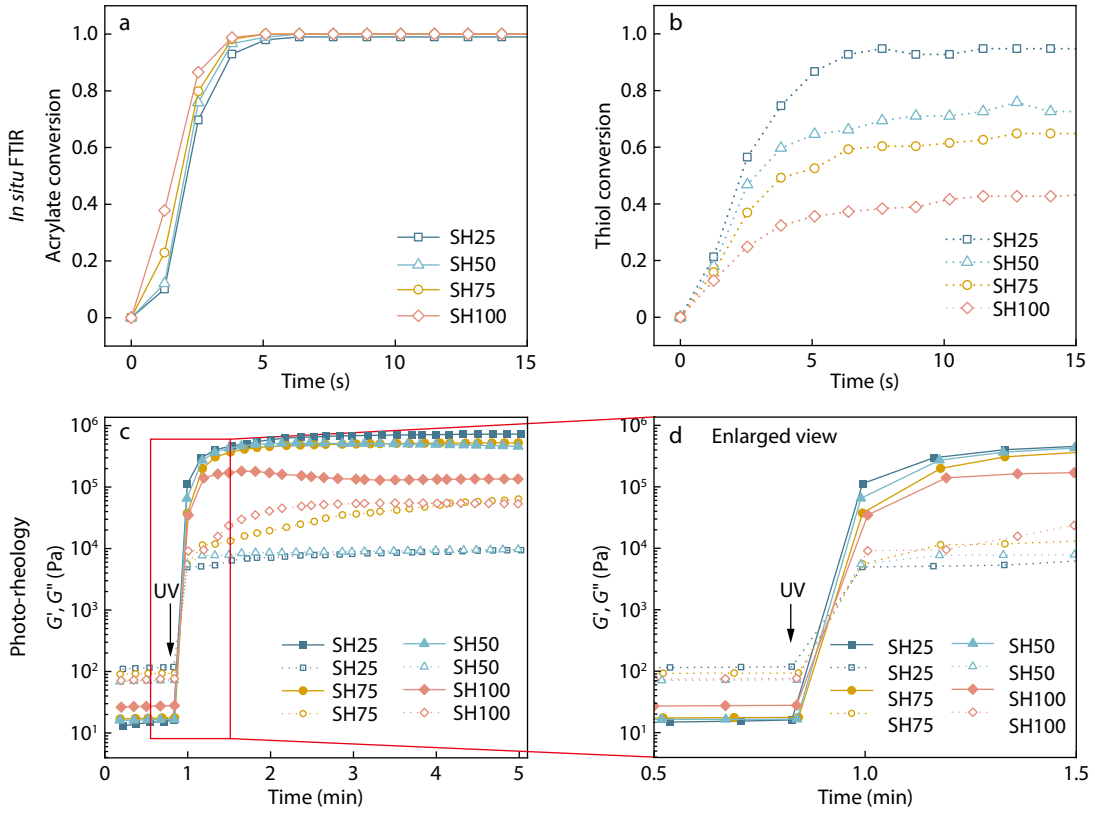

Fig. 3 Reaction and curing kinetics of different mixed inks. (a, b) Reaction kinetics monitored by *in situ* FTIR: (a) acrylate conversion, (b) thiol conversion; (c) Variation of storage modulus G' and loss modulus G'' against time t before and after UV light exposure monitored by *in situ* photo-rheology and (d) enlarged view of G' and G'' in the range of 0.5–1.5 min. The content of photoinitiator TPO-L was 1 wt% and UV light intensity was 50 mW/cm^2.

Table 1 Gel fraction and swelling ratio of cured inks with different content of PEGSH.

Sample	Gel fraction (%)	Swelling ratio (%)
SH25	94.5±0.8	72.4±11.7
SH50	92.2±2.6	124.6±20.6
SH75	87.1±4.4	190.4±26.8
SH100	72.3±1.6	246.2±7.6

ation, leading to the formation of a crosslinked network. As the crosslinking progressed, the system underwent a sol-gel transition and gradually developed a solid-like behavior. In addition, according to the rheological results, the final storage modulus G' of the cured inks decreased gradually with increasing PEGSH content, with the SH25 ink exhibiting the highest value. This was in agreement with previous findings that a higher PEGSH content promoted click reactions in thiol-acrylate polymerization, leading to a looser network and, consequently, lower G' and higher G''.[34,35]

To further evaluate the effect of the PEGSH ratio on the network structure, the gel fraction of the crosslinked network was determined. Table 1 summarizes the gel fractions and swelling ratios of the four cured inks with different PEGSH contents. It could be observed that with increasing thiol content, the gel fraction of the crosslinked networks decreased, while the swelling ratio correspondingly increased. This is due to the higher thiol PEGSH content, which promotes click reactions in thiol-acrylate photopolymerization. As a result, a looser network structure was formed, leading to a reduced gel fraction and an increased swelling ratio (Fig. 4a). It is noteworthy that, except for SH100, the gel fractions of SH25, SH50, and SH75 cured inks all exceeded 80%, indicating a high degree of network integrity. In the case of SH100, excessive PEGSH content increased the likelihood of dangling chains, resulting in more network defects.[36]

Dynamic mechanical analysis (DMA) was employed to characterize the network structures of SH25, SH50, and SH75. Fig. 4(b) and Fig. S5 (in ESI) show the variations in the storage modulus (E'), loss modulus (E'), and tanδ with temperature for the different cured inks. As shown in Fig. 4(c), T_g shifted to lower temperatures with increasing PEGSH content, which can be attributed to the higher proportion of click reactions in the system, leading to a more regular and looser network. Consequently, less thermal energy was required for chain segment mobility, resulting in a decrease in T_g. Moreover, the crosslink density (V_e) and average molecular weight between crosslinks (M_c) of the cured inks were calculated using Eqs. (5) and (6). The results indicated that as the PEGSH content increased, the crosslink density V_e decreased, whereas the average molecular weight between crosslinks M_c increased (Figs. 4b and 4d). The decrease in the crosslink density contributed to the downward shift in T_g, which also explains the observed variations in the gel fraction and swelling ratio. Additionally, the uniformity of the crosslinked network was characterized by the full width at half maximum (FWHM) of the tanδ

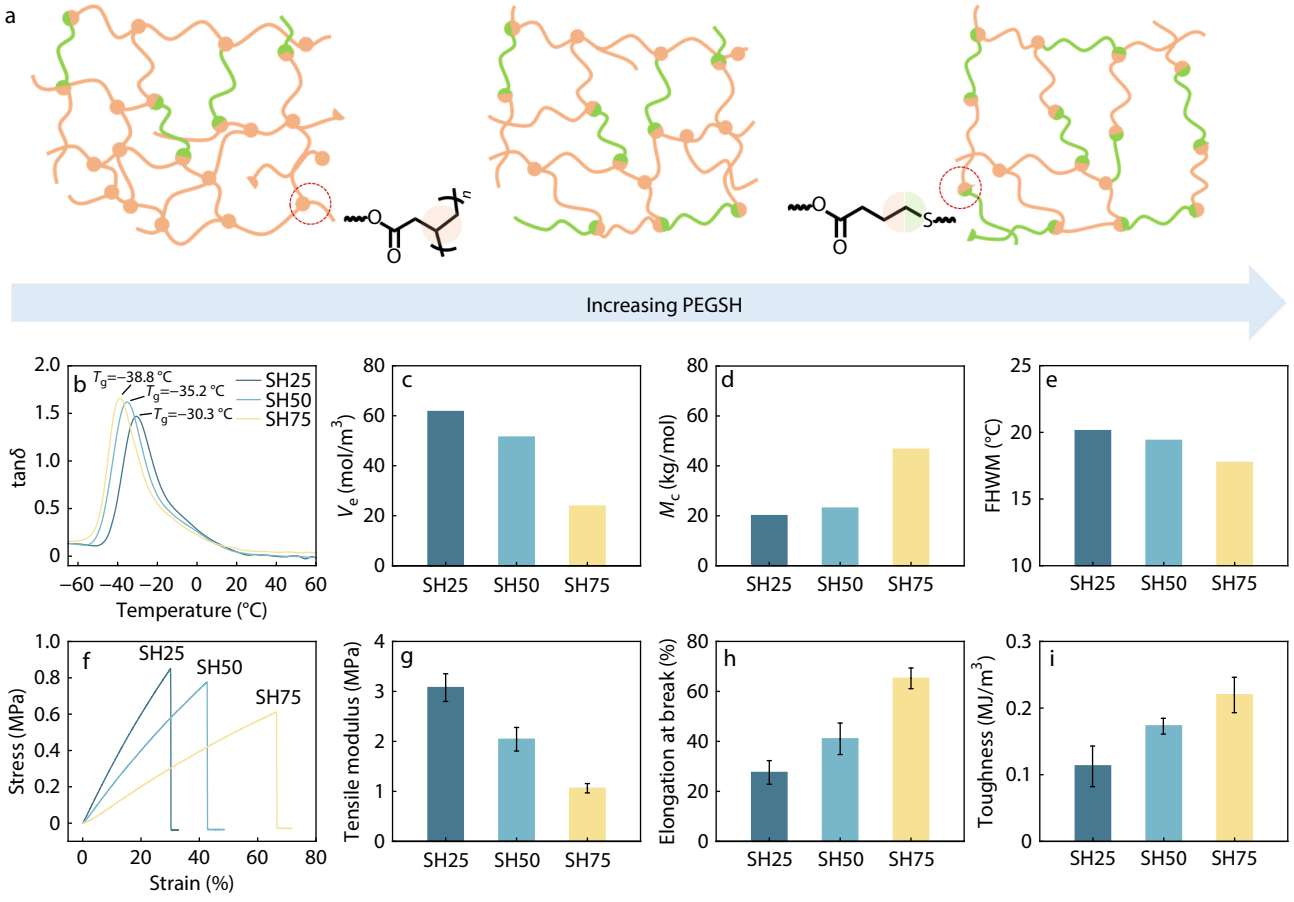

Fig. 4 Network structure and mechanical properties characterization of SH25, SH50, and SH75 cured inks. (a) Schematic illustration of thiol-acrylate network structural evolution with increasing PEGSH content; (b–e) DMA tests of cured inks: (b) comparison of tanδ peaks; (c) crosslinking density (V_e) and (d) average molecular weight between crosslinks (M_c) calculated using Eqs. (5) and (6); (e) full width at half maximum (FWHM) of the tanδ peak. (f–i) Tensile tests of cured inks: (f) stress-strain curves; (g) tensile modulus, (h) elongation at break and (i) toughness calculated from stress-strain curves.

peak.[29] As shown in Fig. 4(e), a higher PEGSH content resulted in a decrease in FWHM, indicating improved network uniformity. Generally, networks formed through click reactions exhibit greater uniformity than those formed *via* radical polymerization.[37] Therefore, the SH75 cured ink exhibited enhanced network uniformity owing to the higher proportion of click reactions, in comparison to SH50 and SH25.

The mechanical properties of the cured inks were also evaluated. Fig. 4(f) shows the stress-strain curves of SH25, SH50, and SH75. As shown in Fig. 4(g), the tensile modulus of the samples decreased with increasing PEGSH content, with SH75 exhibiting the lowest modulus. This was due to the higher thiol content, which increased the distance between the crosslinks and decreased the crosslinking density, leading to a reduced modulus. Additionally, the longer polymer segments between the crosslinks dissipated stress by enhancing chain extensibility under tensile loading. Consequently, the SH75 network exhibited the highest segmental flexibility and deformation. This reduced stress concentration led to a higher elongation at break and enhanced toughness compared to those of SH50 and SH25. (Figs. 4h and 4i).

3D Printing with Optimized Inks

Mixed inks of SH25, SH50, and SH75 were used to print 3D scaffolds using a UV-equipped DIW 3D printer. Fig. 5(a) illustrates the printing process. The 3D models of the scaffolds were designed using the software provided by the printer, and the printing process was performed under real-time UV irradiation with optimized parameters (Table S2 in ESI). The 3D scaffolds printed from the SH75, SH50, and SH25 inks are shown in Figs. 5(b)–5(d), respectively. The pores of the SH25 scaffold exhibited a circular shape, whereas those of the SH50 and SH75 scaffolds largely retained a square geometry. Printability (P_r) was calculated using Eq. (7). For printing inks, a P_r value close to 1 indicates better ink printability.[32] As shown in Fig. 5, with increasing PEGSH content in the formulations, the P_r values approached 1. For SH25, the P_r value of the scaffold pores was 0.83, and for SH50 and SH75, the P_r values were both above 0.9. Owing to the low viscosity of SH25, excessive extrusion of the ink occurs under shear, resulting in circular pores. As the PEGSH content in the ink formulation increased, the corresponding higher viscosity after extrusion effectively mitigated excessive extrusion, with SH75 exhibiting the best printing performance. This suggests that the addition of PEGSH enhances the printability of the mixed ink. The temperature of the print nozzle (T_{Nozzle}) was set to 10 °C to ensure the crystalline state of PEGSH. Furthermore, 3D scaffolds of various shapes and pore sizes were printed us-

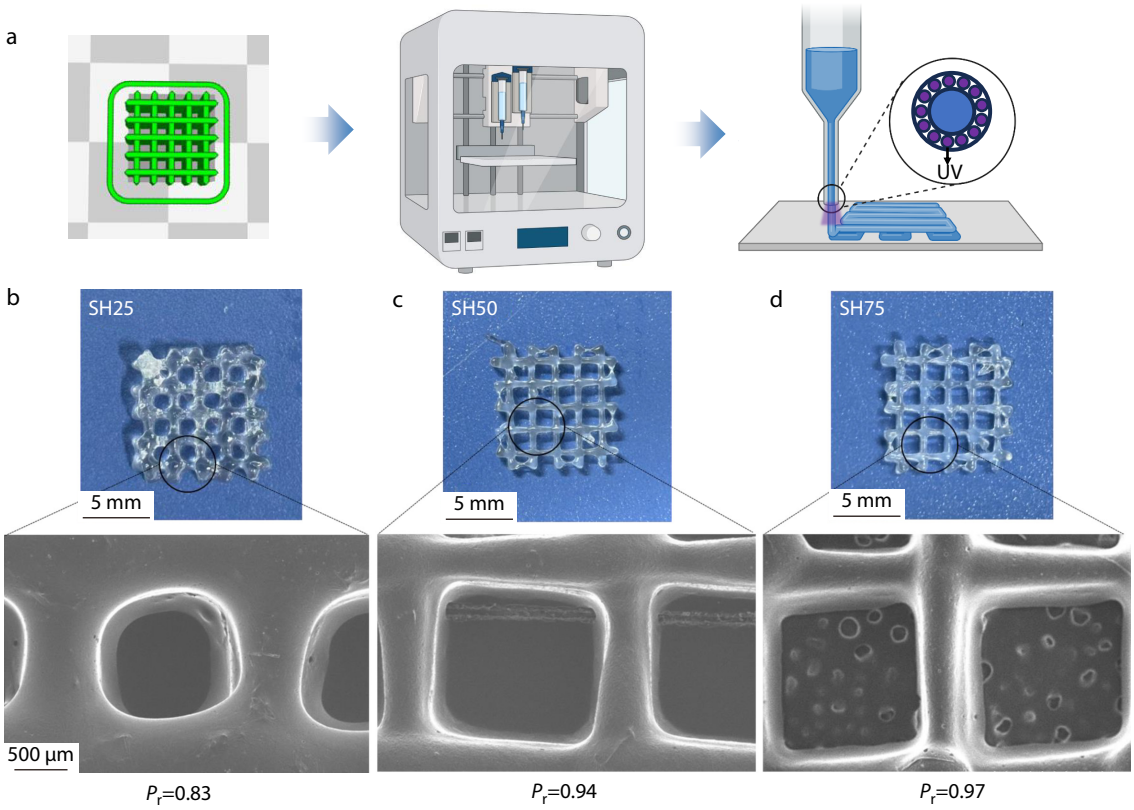

Fig. 5 DLP process. (a) 3D printed model and *in situ* crosslinking strategy; (b–d) Optical images, SEM images and calculate P_r values of printed scaffolds: (b) SH25, (c) SH50 and (d) SH75. The printing speed for three scaffolds was 4 mm/s. The extrusion speed was 0.50 mm^3/s for SH25, 1.00 mm^3/s for SH50, 1.25 mm^3/s for SH75.

ing SH75 (Fig. S7 in ESI). In addition, the formulated ink remained stable over a period of 5 days and could still be used for scaffold printing (Fig. S8 in ESI).

The crystallinity of the printed scaffolds was characterized using X-ray diffraction (XRD). Fig. S9 (in ESI) and Fig. 6(a) show XRD patterns of the SH75 and SH50 inks, as well as the corresponding printed scaffolds. The diffraction peaks at 19.5° and 23.7° in the mixed inks confirm the presence of crystalline structures. After printing, the SH50 and SH75 scaffolds exhibited broad peaks, indicating the presence of amorphous structures. This can be attributed to the disruption of the originally ordered crystalline regions by thiol-acrylate crosslinking, which led to the disappearance of crystalline diffraction peaks.

Moreover, considering that tissues in the body exist in a dynamic environment, the elasticity of the scaffold was evaluated using compression cycle experiments.[38] Fig. 6(b) shows the stress-strain curves of SH50 and SH75 scaffolds after 10 cycles of 50% compression. The loading-unloading curves of the printed scaffolds remained nearly overlapping across the 10 compression cycles. Additionally, the stress-time curves demonstrated that the peak stress in each cycle remained consistent (Fig. 6c). The scaffolds exhibited excellent elasticity and fatigue resistance at room temperature.

The thermal properties of the printed scaffolds were evaluated using TGA and DSC. As shown in Fig. 6(d), no distinct multistep mass loss was observed during heating for either SH75 or SH50 scaffolds. The results suggested that the crosslinked network of the scaffolds was relatively uniform, with no significant phase separation or sequential decomposition of the different structural components. In addition, the initial thermal decomposition temperature ($T_{d,5\%}$) of SH75 scaffold was lower than that of SH50 scaffold. This can be attributed to the increase in PEGSH content, which lowers the crosslink density of the network and reduces its structural stability. The DTG results also revealed that the maximum decomposition temperature ($T_{d,max}$) of the SH50 scaffold was higher than that of the SH75 scaffold (Fig. 6e). Nevertheless, the initial thermal decomposition temperatures of both the SH50 and SH75 scaffolds exceeded 300 °C, indicating excellent thermal stability. This suggests that scaffolds are suitable for use under normal conditions and in tissue engineering applications. The T_g values of the SH50 and SH75 scaffolds determined by DSC were −24.4 and −29.5 °C, respectively, indicating that the scaffolds remained in a rubbery state at room temperature (Fig. S10 in ESI). Moreover, the increase in PEGSH content led to a decrease in the T_g of the scaffolds, which was attributed to the reduced crosslink density. Notably, the T_g values of the scaffold measured by DSC differed from those of the cured ink obtained by DMA, which can be attributed to differences in the measurement principles of the instruments and heating rate. Additionally, the hydrophilicity of the material surface directly influences its interactions with the biological environment, including cell adhesion and degradation.[39]

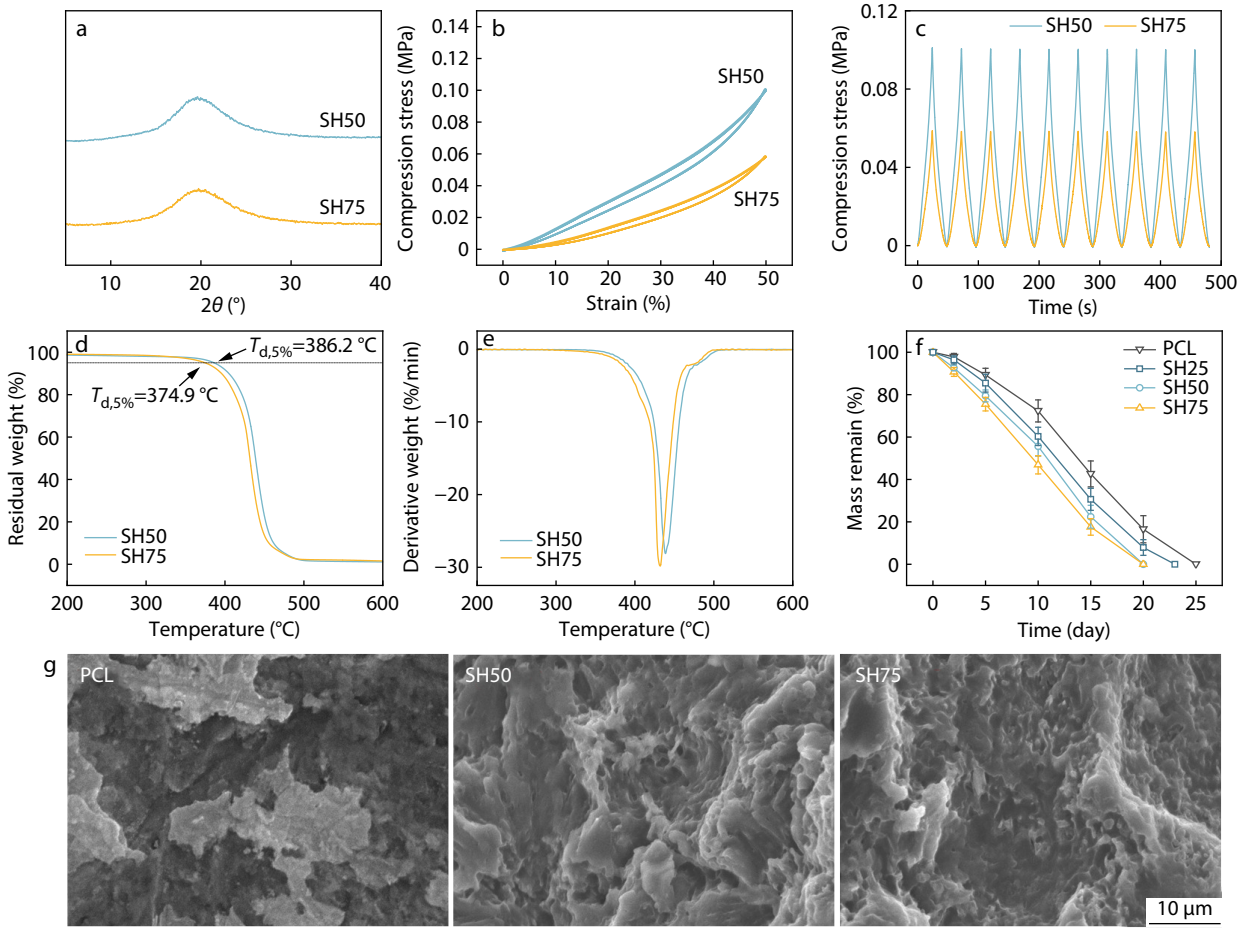

Fig. 6 Characterization of the properties of different scaffolds. (a) XRD patterns of SH50 and SH75 scaffolds; (b) Compressive stress-strain curves for 10 cycles and (c) stress-time curves for 10 cycles of SH50 and SH75 scaffolds; (d) TGA curves and (e) DTG curves of SH50 and SH75 scaffolds; (f) Degradation profiles in lipase-containing PBS solution (250 U/mL). PCL scaffold (M_n=8×10^4) was used as the control; (g) Surface morphologies of SH75, SH50, and PCL scaffolds after 10 days of *in vitro* enzymatic degradation.

Therefore, the surface wettability of the SH75 and SH50 scaffolds was characterized using a contact angle goniometer. As shown in Fig. S11 (in ESI), the contact angle of the SH50 scaffold is higher than that of the SH75 scaffold. The precursor PMCLDA is inherently hydrophobic,[40] and the incorporation of hydrophilic PEGSH reduces the overall hydrophobicity of the scaffold. Consequently, the SH75 scaffold exhibited higher hydrophilicity owing to its higher PEGSH content.

In vitro Degradation Behavior of Scaffolds

In vitro degradation of the SH75 and SH50 scaffolds was conducted in PBS containing lipase (250 U/mL) at 37 °C, with melt-extruded PCL scaffolds (M_n=8×10^4) used as the control group. As shown in Fig. 6(f), the SH50 and SH75 scaffolds completely degraded within 20 days, whereas the PCL scaffold required 25 days for complete degradation. This difference was attributed to the fact that the amorphous regions of the polymers are more susceptible to hydrolysis than the crystalline regions, which results in a slower degradation rate of PCL.[41] Moreover, the degradation rate of SH75 was faster than that of SH50, which could be attributed to the higher PEGSH content enhancing the hydrophilicity of the scaffolds. Additionally, the lower crosslink density of SH75 facilitates the penetration of water and enzymes, thereby accelerating the degradation process. SEM images of the scaffolds after 10 days of enzymatic degradation are shown in Fig. 6(g). The surface of the SH75 scaffold showed the most severe erosion, whereas the PCL scaffold showed the least erosion.

Cytocompatibility of Scaffolds

The cytocompatibility of the SH50, SH75, and PCL scaffolds was assessed using *in vitro* cytotoxicity and cell proliferation assays. Cell viability was assessed using the CCK-8 assay. Fig. 7(a) illustrates the viability of the L929 cells on Days 1, 3, and 7. It can be observed that the cell viability on the printed scaffold remained stable, with no significant decline. Additionally, the cell viability of the SH50 and SH75 scaffolds was comparable to that of the control and PCL groups, indicating that the scaffold exhibited no significant cytotoxicity.

To further evaluate the effect of the scaffolds on cell proliferation, the SH75, SH50, and PCL scaffolds were co-cultured with L929 cells for 7 days. As shown in Fig. 7(b), the OD values of the L929 cells cultured on all three scaffolds increased over time, indicating that the scaffolds promoted cell proliferation. Moreover, the cell viability on the SH75 scaffold was higher than that on PCL and SH50, which can be attributed to the higher hydrophilicity of the scaffold, facilitating cell adhesion. Additionally, the green fluorescence intensity in the

https://doi.org/10.1007/s10118-026-3582-0

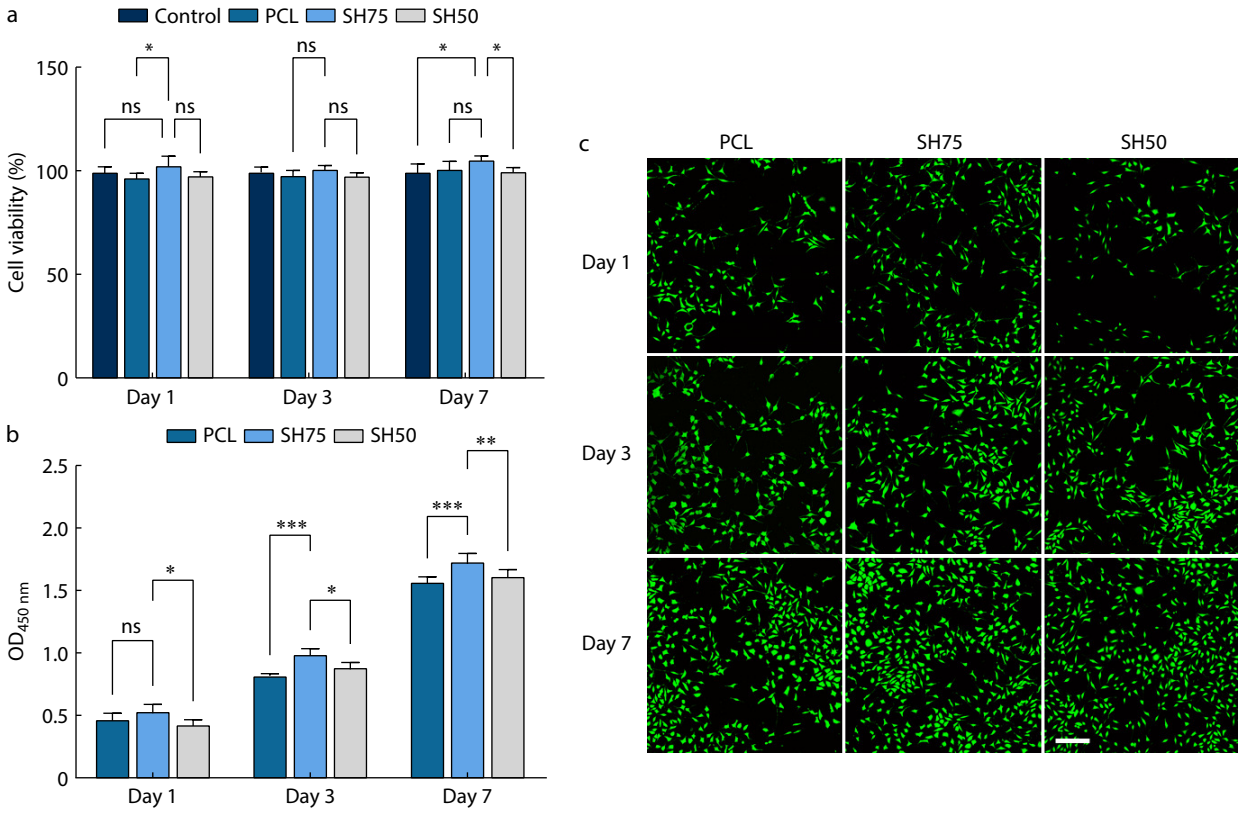

Fig. 7 *In vitro* cytocompatibility assessments. (a) Cell viability of L929 on Days 1, 3 and 7; (b) OD values of SH75, SH50 and PCL scaffolds co-culture with L929 cells for 1, 3 and 7 days. $^{*}p<0.05$, $^{**}p<0.01$, $^{***}p<0.001$. (c) Live and dead cell staining merged images of scaffold SH75, SH50 and PCL co-cultured with L929 cells for 1, 3, 7 days. Scale bar: 200 μm.

live/dead staining images increased over time on Days 1, 3, and 7, whereas red fluorescence corresponding to dead cells was barely observed (Fig. 7c). These results demonstrate that the 3D-printed scaffolds possessed excellent cytocompatibility.

CONCLUSIONS

In summary, thiol-functionalized PEGSH was used as a rheological modifier in combination with the liquid precursor PMCLDA to prepare DIW inks for elastic and biodegradable 3D scaffolds. The incorporation of PEGSH imparted shear-thinning behavior to the mixed ink, thereby facilitating smooth extrusion through the printing nozzle. Furthermore, efficient thiol-acrylate photopolymerization enabled the rapid crosslinking of the ink after extrusion, preserving the structural precision of the scaffolds. The crosslinked network of the cured inks can be tuned by adjusting the PEGSH feeding ratio. Increasing the PEGSH content reduces the crosslinking density and results in a more uniform network topology. In addition, various inks were demonstrated to be printable under appropriate printing parameters, with SH75 exhibiting the best printability. The 3D printed scaffolds displayed excellent elasticity and were biodegradable during the enzymatic degradation. *In vitro* cell assays confirmed the cytocompatibility of the scaffolds and their ability to support cell growth, particularly the SH75 scaffold. Therefore, printed elastic, biodegradable, and cytocompatible 3D scaffolds have significant potential for tissue-engineering applications.

Conflict of Interests

The authors declare no interest conflict.

Electronic Supplementary Information

Electronic supplementary information (ESI) is available free of charge in the online version of this article at http://doi.org/10.1007/s10118-026-3582-0.

Data Availability Statement

The data supporting the findings of this study are available from the corresponding author upon reasonable request.

ACKNOWLEDGMENTS

This work was financially supported by the National Key Research and Development Program (No. 2021YFB3800800) and the National Natural Science Foundation of China (No. 52273009).

REFERENCES

1 Gillispie, G.; Prim, P.; Copus, J.; Fisher, J.; Mikos, A. G.; Yoo, J. J.; Atala, A.; Lee, S. J. Assessment methodologies for extrusion-based bioink printability. *Biofabrication* **2020**, *12*, 022003.

Graphical Abstract

Direct Ink Writing of Biodegradable Elastic Scaffolds *via* Rapid Thiol-Acrylate Photocrosslinking

Xiao-Yu Li , Chong-Guang Li, Kai Chen, Yan Xiao, Xin-Xin Li, and Mei-Dong Lang

East China University of Science and Technology

The incorporation of thiol-functionalized poly(ethylene glycol) (PEGSH) into acrylate-functionalized liquid poly(4-methyl-ε-caprolactone) (PMCLDA) precursor afforded the mixed inks shear thinning behavior. The network structure of scaffolds was regulated by thiol-acrylate photopolymerization.

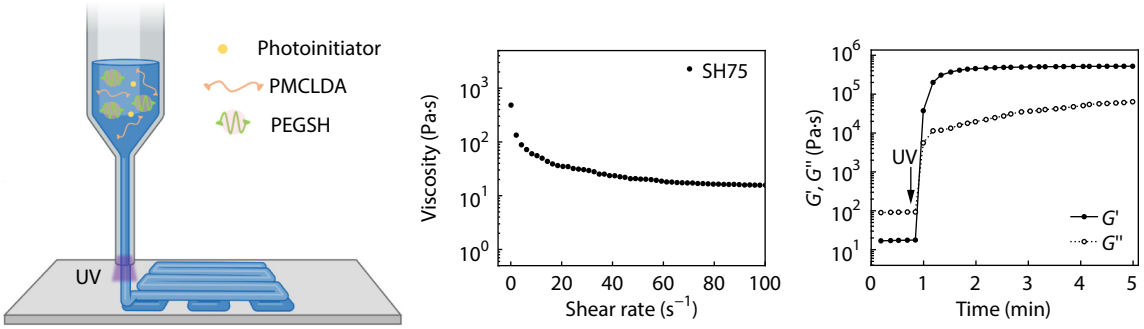

Chinese J. Polym. Sci., 2026 *https://doi.org/10.1007/s10118-026-3582-0*

2 Yuan, X.; Zhu, W.; Yang, Z.; He, N.; Chen, F.; Han, X.; Zhou, K. Recent advances in 3D printing of smart scaffolds for bone tissue engineering and regeneration. *Adv. Mater.* **2024**, *36*, 2403641
3 Sadeghianmaryan, A.; Ahmadian, N.; Wheatley, S.; Alizadeh, S. H.; Nasrollah, S. A. S.; Naseri, E.; Ahmadi, A. Advancements in 3D-printable polysaccharides, proteins, and synthetic polymers for wound dressing and skin scaffolding — a review. *Int. J. of Biol. Macromol.* **2024**, *266*, 131207
4 Ligon, S. C.; Liska, R.; Stampfl, J.; Gurr, M.; Mülhaupt, R. Polymers for 3D printing and customized additive manufacturing. *Chem. Rev.* **2017**, *117*, 10212−10290.
5 Truby, R. L.; Lewis, J. A. Printing soft matter in three dimensions. *Nature* **2016**, *540*, 371−378.
6 Chartrain, N. A.; Williams, C. B.; Whittington, A. R. A Review on fabricating tissue scaffolds using vat photopolymerization. *Acta Biomater.* **2018**, *74*, 90−111.
7 Zhang, M.; Lin, R.; Wang, X.; Xue, J.; Deng, C.; Feng, C.; Zhuang, H.; Ma, J.; Qin, C.; Wan, L.; Chang, J.; Wu, C. 3D Printing of haversian bone-mimicking scaffolds for multicellular delivery in bone regeneration. *Sci. Adv.* **2020**, *6*, eaaz6725.
8 Zhu, S.; Liao, X.; Xu, Y.; Zhou, N.; Pan, Y.; Song, J.; Zheng, T.; Zhang, L.; Bai, L.; Wang, Y.; Zhou, X.; Gou, M.; Tao, J.; Liu, R. 3D Bioprinting of high-performance hydrogel with in-situ birth of stem cell spheroids. *Bioact. Mater.* **2025**, *43*, 392-405.
9 Wang, W.; Zhang, B.; Li, M.; Li, J.; Zhang, C.; Han, Y.; Wang, L.; Wang, K.; Zhou, C.;Liu, L.; Fan, Y.; Zhang, X. 3D Printing of PLA/n-HA Composite scaffolds with customized mechanical properties and biological functions for bone tissue engineering. *Compos. Part B Eng.* **2021**, *224*, 109192.
10 Cano-Vicent, A.; Tambuwala, M. M.; Hassan, S. S.; Barh, D.; Aljabali, A. A. A.; Birkett, M.; Arjunan, A.; Serrano-Aroca, Á. fused deposition modelling: current status, methodology, applications and future prospects. *Addit. Manuf.* **2021**, *47*, 102378.
11 Baniasadi, H.; Abidnejad, R.; Fazeli, M.; Lipponen, J.; Niskanen, J.; Kontturi, E.; Seppälä, J.; Rojas, O. J. Innovations in hydrogel-based manufacturing: a comprehensive review of direct ink writing technique for biomedical applications. *Adv. Colloid Interface Sci.* **2024**, *324*, 103095.
12 Ajdary, R.; Huan, S.; Zanjanizadeh Ezazi, N.; Xiang, W.; Grande, R.; Santos, H. A.; Rojas, O. J. Acetylated nanocellulose for single-component bioinks and cell proliferation on 3D-printed scaffolds. *Biomacromolecules* **2019**, *20*, 2770−2778.
13 Rau, D. A.; Williams, C. B.; Bortner, M. J. Rheology and printability: a survey of critical relationships for direct ink write materials design. *Prog. Mater. Sci.* **2023**, *140*, 101188.
14 Zhou, Y.; Wei, G.; Yuan, J.; Sang, X.; Miao, J. T.; Liu, R. UV-assisted direct ink writing 4D printing of benzoxazine/epoxy thermosets. *Chem. Eng. J.* **2023**, *477*, 147221.
15 Zhang, B.; Chung, S. H.; Barker, S.; Craig, D.; Narayan, R. J.; Huang, J. Direct ink writing of polycaprolactone/polyethylene oxide based 3D constructs. *Prog. Nat. Sci. Mater. Int.* **2021**, *31*, 180−191.
16 Lei, D.; Yang, Y.; Liu, Z.; Chen, S.; Song, B.; Shen, A.; Yang, B.; Li, S.; Yuan, Z.; Qi, Q.; Sun, L.; Guo, Y.; Zuo, H.; Huang, S.; Yang, Q.; Mo, X.; He, C.; Zhu, B.; Jeffries, E. M.; Qing, F.-L.; Ye, X.; Zhao, Q.; You, Z. A general strategy of 3D printing thermosets for diverse applications. *Mater. Horiz.* **2019**, *6*, 394−404.
17 Hausladen, M. M.; Gorbea, G. D.; Francis, L. F.; Ellison, C. J. UV-assisted direct ink writing of dual-cure polyurethanes. *ACS Appl. Polym. Mater.* **2024**, *6*, 2253−2265.
18 Liu, B.; Duan, T.; Wang, T.; Ren, X.; Gao, G. Direct ink-writable tough polyurethane acrylate elastomers for underwater intelligent monitoring equipment. *Chem. Eng. J.* **2025**, *509*, 161448.
19 Li, Y.; Liu, T.; Ambrogi, V.; Rios, O.; Xia, M.; He, W.; Yang, Z. Liquid crystalline elastomers based on click chemistry. *ACS Appl. Mater. Interfaces* **2022**, *14*, 14842−14858.

20 O'Brien, A. K.; Cramer, N. B.; Bowman, C. N. Oxygen inhibition in thiol-acrylate photopolymerizations. *J. Polym. Sci. A Polym. Chem.* **2006**, *44*, 2007–2014.
21 Blasco, E.; Wegener, M.; Barner-Kowollik, C. Photochemically driven polymeric network formation: synthesis and applications. *Adv. Mater.* **2017**, *29*, 1604005.
22 Xiao, Y.; Lang, S.; Zhou, M.; Qin, J.; Yin, R.; Gao, J.; Heise, A.; Lang, M. A highly stretchable bioelastomer prepared by UV curing of liquid-like poly(4-methyl-epsilon-caprolactone) precursors. *J. Mater. Chem. B.* **2017**, *5*, 595–603.
23 Xiao, Y.; Zhou, M. M.; Zhang, Liu, W.; Zhou, Y.; Lang, M.; Hepatocyte culture on 3D porous scaffolds of PCL/PMCL, *Colloids Surf. B Biointerfaces* **2019**, *173*, 185-193.
24 Watts, A.; Kurokawa, N.; Hillmyer, M. A. Strong, resilient, and sustainable aliphatic polyester thermoplastic elastomers. *Biomacromolecules* **2017**, *18*, 1845–1854.
25 Cai, X. Y.; Li, J. Z.; Li, N. N.; Chen, J. C.; Kang, E. T.; Xu, L. Q. PEG-based hydrogels prepared by catalyst-free thiol-yne addition and their post-antibacterial modification. *Biomater. Sci.* **2016**, *4*, 1663–1672.
26 Panja, S.; Siehr, A.; Sahoo, A.; Siegel, R. A.; Shen, W. Biodegradable elastomers enabling thermoprocessing below 100 °C. *Biomacromolecules* **2021**, *23*, 163–173.
27 Huang, W.; Xiao, Y.; Yin, W.; Yang, S.; Lang, M. An engineered cardiac patch based on biodegradable thermoplastic elastomer fabricated by 3D printing and *in situ* polymerization. *Eur. Polym. J.* **2024**, *209*, 112890.
28 Li, X.; Ren, N.; Xiao, Y.; Li, X.; Lang, M.; Zhu, X. Construction and regulation on thiol-acrylate networks through binary polymerization of thiol-ene polymerization and free radical polymerization. *Macromolecules* **2024**, *57*, 9867–9876.
29 Thijssen, Q.; Parmentier, L.; Augustyniak, E.; Mouthuy, P. A.; Van Vlierberghe, S. From chain growth to step growth polymerization of photoreactive poly-ε-caprolactone: the network topology of bioresorbable networks as tool in tissue engineering. *Adv. Funct. Mater.* **2022**, *32*, 2108869.
30 Ivanoff, D. G.; Sung, J.; Butikofer, S. M.; Moore, J. S.; Sottos, N. R. Cross-linking agents for enhanced performance of thermosets prepared *via* frontal ring-opening metathesis polymerization. *Macromolecules* **2020**, *53*, 8360–8366.
31 Ding, R.; Xia, Y.; Mauldin, T. C.; Kessler, M. R. Biorenewable ROMP-based thermosetting copolymers from functionalized castor oil derivative with various cross-linking agents. *Polymer* **2014**, *55*, 5718–5726.
32 Ouyang, L.; Yao, R.; Zhao, Y.; Sun, W. Effect of bioink properties on printability and cell viability for 3D bioplotting of embryonic stem cells. *Biofabrication* **2016**, *8*, 035020.
33 Pielichowski, K.; Flejtuch, K. Differential scanning calorimetry studies on poly(ethylene glycol) with different molecular weights for thermal energy storage materials. *Polym. Adv. Technol.* **2003**, *13*, 690–696.
34 Cramer, N. B.; Reddy, S. K.; O'Brien, A. K.; Bowman, C. N. Thiol-ene photopolymerization mechanism and rate limiting step changes for various vinyl functional group chemistries. *Macromolecules* **2003**, *36*, 7964–7969.
35 Roquart, M.; Kharlamova, A.; Marcos, C. L.; Norvez, S.; Nicolay, R.; Corte, L. PEG-based photo-cross-linked networks with adjustable topologies and mechanical properties. *Biomacromolecules* **2023**, *24*, 4454–4464.
36 Hebner, T. S.; Fowler, H. E.; Herbert, K. M.; Skillin, N. P.; Bowman, C. N.; White, T. J. Polymer network structure, properties, and formation of liquid crystalline elastomers prepared *via* thiol-acrylate chain transfer reactions. *Macromolecules* **2021**, *54*, 11074–11082.
37 Seiffert, S. Origin of Nanostructural inhomogeneity in polymer-network gels. *Polym. Chem.* **2017**, *8*, 4472–4487.
38 Zhang, P.; Liu, X.; Guo, P.; Li, X.; He, Z.; Li, Z.; Stoddart, M. J.; Grad, S.; Tian, W.; Chen, D.; Zou, X.; Zhou, Z.; Liu, S. Effect of Cyclic Mechanical loading on immunoinflammatory microenvironment in biofabricating hydroxyapatite scaffold for bone regeneration. *Bioact. Mater.* **2021**, *6*, 3097–3108.
39 Rydholm, A. E.; Bowman, C. N.; Anseth, K. S. Degradable Thiol-acrylate photopolymers: polymerization and degradation behavior of an *in situ* forming biomaterial. *Biomaterials* **2005**, *26*, 4495–506.
40 Wang, Z.; Zhang, W.; Bai, G.; Lu, Q.; Li, X.; Zhou, Y.; Yang, C.; Xiao, Y.; Lang, M. Highly resilient and fatigue-resistant poly(4-methyl-ε-caprolactone) porous scaffold fabricated *via* thiol-yne photo-crosslinking/salt-templating for soft tissue regeneration. *Bioact. Mater.* **2023**, *28*, 311–325.
41 Lam, C. X. F.; Teoh, S. H.; Hutmacher, D. W. Comparison of the degradation of polycaprolactone and polycaprolactone-(β-tricalcium phosphate) scaffolds in alkaline medium. *Polym. Int.* **2007**, *56*, 718–728.

https://doi.org/10.1007/s10118-026-3582-0